Handling partially calibrated conformal antenna arrays in range−dependence compensation for airborne bistatic space−time adaptive processing radar

P. Ries[1] F.D. Lapierre[2] M. Lesturgie[3] J.G. Verly[1]

[1]Department of Electrical Engineering and Computer Science, University of Liège, Sart-Tilman, Building B28, B-4000 Liège, Belgium
[2]CISS Department, Royal Military Academy, Avenue de la Renaissance 30, B-1000 Brussels, Belgium
[3]ONERA, Chemin de la Hunière et des Joncherettes, 91120 Palaiseau, France
E-mail: ries@montefiore.ulg.ac.be

Abstract: The authors consider space−time adaptive processing (STAP) when the radar returns are recorded by a conformal antenna array (CAA). The statistics of the secondary data snapshots used to estimate the optimum weight vector are not identically distributed with respect to range, thus preventing the customary STAP processor from achieving its optimum performance. The compensation of the range dependence of the secondary data requires precise knowledge of the array response for any direction of arrival (DOA), and, thus, of the spatial steering vectors (SVs). The authors propose a novel registration-based range-dependence compensation algorithm that gives an accurate estimate of the interference-plus-noise covariance matrix under the hypotheses that calibrated spatial SVs are available only for a small set of DOAs, and that the errors in the model giving the true spatial SV for each DOA are DOA dependent. The performance in terms of signal-to-interference-plus-noise ratio loss is promising.

1 Introduction

Space−time adaptive processing (STAP) is a powerful technique for detecting slow-moving targets against a strong-interference background [1−3]. STAP relies on an antenna array of N elements and a train of M coherent pulses. The data recorded by STAP radars can be seen as a sequence, in range, of $NM \times 1$ vectors, called snapshots. For each range, the optimum processor (OP) computes an optimum weighted linear combination of the snapshot elements to determine whether a target is present or not at that range. In practice, the interference-plus-noise (I + N) covariance matrix (CM) needed for the computation of the optimum filter must be estimated from snapshots at neighbouring ranges; these snapshots constitute the secondary data.

Unfortunately, the secondary-data snapshots are typically not identically distributed with respect to range [4].

Therefore the method proposed in [5] for estimating the I + N CM from the secondary data is not applicable here. Indeed, the estimator proposed in [5] is maximum likelihood only if the secondary data snapshots are independent and identically distributed. There are two major reasons for which the secondary data are not identically distributed. The first reason is clutter heterogeneity which is described in [6]. Several, mostly knowledge-aided, techniques have been investigated to mitigate the impact of clutter heterogeneity [7−12]. The second reason is the geometry-induced variation of clutter signature with range. The clutter signature at a given range and, thus, the required response of the optimum space−time filter, are determined by the geometry of the structure of the receiver array, its geometrical orientation with respect to its carrying platform, and the relative orientation of the receiver and the transmitter in the case of a bistatic (BS) configuration [13−15]. This clutter signature depends on

range and makes it unacceptable to estimate the I + N CM by simply averaging the sample CMs corresponding to the secondary-data snapshots. A STAP filter neglecting the range-dependent statistics of the secondary data leads to a severe reduction in detection performance. This problem is called the geometry-induced range-dependence (RD) problem or simply the RD problem, and the secondary data are said to be range dependent. The present paper addresses the RD problem and offers a novel solution to this problem in the case of conformal antenna arrays (CAAs) that are not perfectly calibrated and that operate in BS configurations.

Early STAP architectures considered monostatic (MS) flight configurations and uniform linear arrays (ULAs), generally in sidelooking positions. For these simple situations, the impact of range-varying clutter signature is negligible [1]. For STAP systems with ULAs operating in BS configurations, the evolution of the clutter signature with range becomes more complicated and RD compensation algorithms are required [16–22]. The growing interest in applying STAP, whether in MS or BS configurations, to CAAs leads to even more complex clutter signatures. The advantages of CAAs, such as preservation of the aerodynamic properties of the carrying platform, can thus only be obtained at the cost of more advanced RD compensation algorithms [23–25].

The growing interest in CAAs has contributed to the development of RD compensation algorithms for CAAs. The registration-based range-dependence compensation (RBC) algorithm presented in [14, 15] allows one to obtain a CM estimate not suffering from RD. The algorithms described in [26–28] provide similar results. However, these algorithms all assume that the 'true' spatial steering vectors (SVs) (defined later) are available for all possible directions of arrival (DOAs), that is, that the array is completely calibrated. In [29], we presented a method performing accurate RBC with the spatial SVs assumed calibrated for all DOAs, except for unknown, DOA-independent, gain and phase errors on each antenna element.

This paper makes the more realistic assumptions that the true spatial SVs are available only for a small number of DOAs (e.g. obtained through calibration), and that the errors in the model (defined later) giving the true spatial SVs for each DOA are DOA-dependent. Our contribution is an array-interpolation based approximation scheme tailored to our RBC algorithm that allows one to perform, under these assumptions, an accurate RBC, leading to a valid I + N CM estimate. The impact of SV mismatch is examined in [30], but no solution to the problem is proposed. The authors of [9, 31] propose several techniques to obtain the true spatial SVs, but these techniques focus on finding the spatial SVs in the direction of the peak clutter returns. On the contrary, our method, although not being a self-calibration method, allows one, under the given assumptions, to synthesise valid approximations of the

'missing' true spatial SVs for any DOA leading to very promising end-to-end STAP performance for CAAs operating in BS configurations.

Section 2 introduces the signal model used in this paper. Section 3 describes the RD problem. Section 4 introduces our new RBC method. Section 5 gives results. Section 6 concludes.

2 Signal model

Fig. 1 describes the generic BS configuration used throughout this paper. It is characterised by the position (x_R, y_R, z_R) of the receiver (R) relative to the transmitter (T), the transmitter velocity v_T, the receiver velocity v_R, the angle α_R between the velocity vectors (assumed horizontal) of the receiver and the transmitter, and the crab angle δ.

One of the signal models used in this paper to describe the space–time snapshot is a simplified version of that used by Hersey *et al.* [32]. A single scatterer S characterised by a DOA (θ, ϕ), with corresponding spatial frequency vector [15]

$$\nu_s(\theta, \phi) = 0.5[\cos\theta\cos(\phi - (\delta + \alpha_R)),$$
$$\cos\theta\sin(\phi - (\delta + \alpha_R)), -\sin\theta]^T \quad (1)$$

where T denotes transpose, and by a normalised Doppler frequency ν_d, gives rise to the space–time snapshot [15]

$$y = \sigma[a_t(\nu_d) \odot s_t(\nu_d)] \otimes [a_s(\nu_s) \odot s_s(\nu_s)]$$

where $\otimes$ is the Kronecker product and $\odot$ is the element-wise product. σ is a complex-valued random amplitude, and a_t and a_s are random vectors modelling the temporal and spatial decorrelations, respectively. The general expression for the temporal SV $s_t(\nu_d)$ is

$$s_t(\nu_d) = \left[1 \; e^{j2\pi\nu_d} \cdots e^{j2\pi\nu_d(M-1)}\right]^T \quad (2)$$
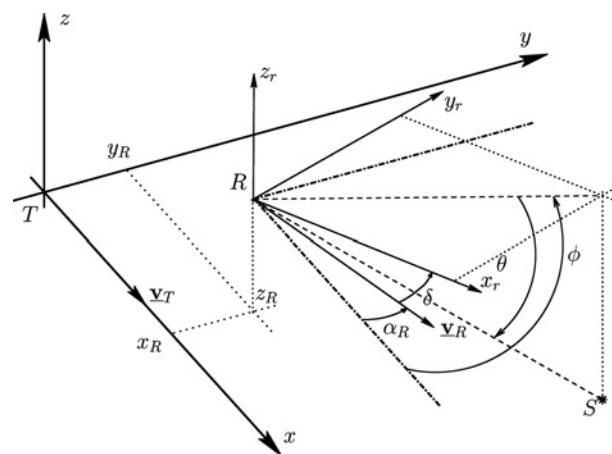

Figure 1 *BS configuration: transmitter T, receiver R and scatterer S*

and that for the spatial SV $s_s(\nu_s)$ is

$$
s_s(\nu_s) = \left[\sqrt{g_0(\theta, \phi)} \, e^{j(2\pi \nu_s^T p(0))/(\lambda/2)} \cdots \right.
$$
$$
\left. \sqrt{g_{N-1}(\theta, \phi)} \, e^{j(2\pi \nu_s^T p(N-1))/(\lambda/2)} \right]^T \quad (3)
$$

where $p(n)$ is the position vector of the nth antenna element, λ is the wavelength at the carrier frequency and $g_n(\theta, \phi)$ is the gain of the nth antenna element for DOA (θ, ϕ). For simplicity, we do not consider range ambiguities.

The clutter snapshot corresponding to a given range cell k is obtained by coherently summing the statistically independent contributions of all Q clutter patches (indexed by i) located in this range cell, that is

$$
y_{c,k} = \sum_{i=0}^{Q-1} \sigma_{k,i} \big[a_t(\nu_{d,i}) \odot s_t(\nu_{d,i}) \big] \otimes \big[a_s(\nu_{s,i}) \odot s_s(\nu_{s,i}) \big]
$$

We continue with a discussion of the several types of spatial SVs used below: the operational spatial SVs occurring in the real conditions of a mission; the calibrated spatial SVs occurring in the real condition of the calibration phase of the array (e.g. in an anechoic chamber); and the approximation of these spatial SVs obtained via the use of several models. Note that, here, we do not distinguish between operational and calibrated spatial SVs, and thus we refer to both as true spatial SVs. Details are as follows.

A true spatial SV for an arbitrary DOA (θ, ϕ) characterised by $\nu_s \equiv \nu_s(\theta, \phi)$ is denoted by $s_s^{true} = s_s^{true}(\nu_s) = s_s^{true}(\theta, \phi)$ (as appropriate). In the remainder of this paper, we assume that the s_s^{true}'s are available only for a discrete set $\mathcal{S}_d$ of DOAs. The corresponding set $\mathcal{S}$ of s_s^{true}'s is referred to as the calibration table. These true spatial SVs may have been obtained, for example, by calibrating the array only every $\Delta\theta$ degree in elevation and every $\Delta\phi$ degree in azimuth. We then say that the array has been partially calibrated. The set S_d is illustrated in Fig. 2. It is important to note that, in the expression of the theoretical clutter CM used as benchmark in SINR loss computations, one must use the s_s^{true}'s for the required DOAs.

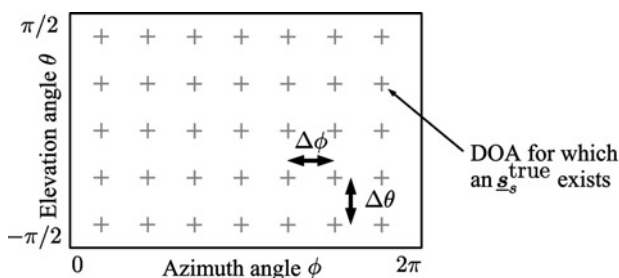An approximated, or model-induced, spatial SV for an arbitrary DOA (θ, ϕ) characterised by $\nu_s = \nu_s(\theta, \phi)$ is denoted by $s_s^{mod} = s_s^{mod}(\nu_s) = s_s^{mod}(\theta, \phi)$. The various models used for generating the s_s^{mod}'s provide different degrees of realism. Each model can be seen as an operator $\mathcal{M}(\cdot, \cdot)$ the input of which is a DOA (θ, ϕ), and the output of which is the corresponding model-induced spatial SV, that is, $s_s^{mod}(\theta, \phi)$. For some models, $\mathcal{M}(\cdot, \cdot)$ is an analytical formula. An analytical model was already given in (3). Section 5 presents another analytical model in (9), which is a simplified version of (3). For some other models, $\mathcal{M}(\cdot, \cdot)$ can be an algorithm, for example, a numerical electromagnetic-simulation tool like FEKO [33].

Carefully note that, while the s_s^{true}'s are available only for a limited number of DOAs, we assume that $\mathcal{M}(\cdot, \cdot)$ allows one to compute the s_s^{mod}'s for any DOA.

3 RD for CAAs

3.1 RD phenomenon

The RD phenomenon for CAAs is best illustrated using the spectral representation for space–time signals recorded by CAAs that was introduced in [15, 23]. The clutter patches contributing to the ground clutter in a snapshot in a given range cell are located on the corresponding isorange. The signal returned by each clutter patch along this isorange is characterised by a particular pair (ν_s, ν_d) of normalised spatial and Doppler frequencies. Hence, the signal from each clutter patch corresponds to a particular point in the 4D spatio-temporal frequency domain (ν_s, ν_d). Each snapshot is the result of the contributions of all the clutter patches along the corresponding isorange. Thus, for each particular range cell, the support of the clutter power spectrum (PS) in the 4D spatio-temporal frequency domain (ν_s, ν_d) is represented by a continuous curve. This 4D curve is called the 4D clutter PS locus [15]. This curve is a very useful tool for investigating the behaviour of the clutter signature with range. This is shown in Fig. 3 for a BS flight configuration. We clearly see that the clutter snapshots are range dependent. This RD gives rise to
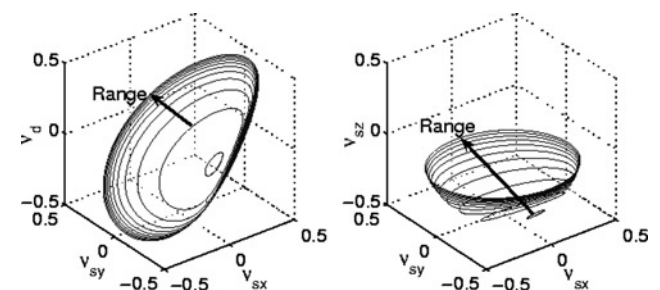

Figure 2 *Set S_d corresponding to the calibration table*

Figure 3 *Evolution of the 4D clutter PS locus for increasing range in a BS configuration*

The first graph is the projection of the 4D clutter PS locus in the $(\nu_{sx}, \nu_{sy}, \nu_d)$ subspace; the second graph is the projection in the $(\nu_{sx}, \nu_{sy}, \nu_{sz})$ subspace. Note that ν_{sx}, ν_{sy} and ν_{sz} are the elements of the normalised spatial frequency vector ν_s

severely biased estimates of the clutter CM when one simply uses an average of sample CMs [15].

3.2 Registration-based RD compensation

Several RD compensation algorithms exist, for example, Doppler warping (DW) [16], angle-Doppler compensation (ADC) [34], adaptive angle-Doppler compensation (A²DC) [18], derivative-based updating (DBU) [21] and RBC [35]. The DW, ADC and A²DC methods have poor performance when used with omnidirectional transmit antennas. The reason is that they register the clutter PS only at a single point. The DBU method relies on the assumption of a linear variation with range of the optimum weight vector and imposes a substantial increase in computational load and in the need for secondary data. The problems associated with the first four methods discussed above are addressed by the RBC algorithm [15, 29, 35], and this is why we choose to extent the RBC algorithm to work under the hypothesis of a partially calibrated array.

Here, we simply recall the elements of the RBC algorithm that are vital to understanding the problem discussed in this paper. The RBC algorithm relies on three steps. (A) An analysis step, where a clutter PS estimate of the snapshot at each range is independently computed along the clutter PS locus at this range. This can be achieved by using a matched filter [35], a least-square fitting technique, a minimum-variance distortionless-response beamformer [24] or a maximum-likelihood estimator [28]. However, these techniques all require precise knowledge of the true space–time SVs (and, thus, of the true spatial SV) for each of the (ν_s, ν_d)-pairs for which a clutter PS estimate is to be obtained. (B) A registration step, where the PS estimates at different ranges are averaged along so-called flowlines (defined in [35]). (C) A synthesis step, where the CM at each range of interest is synthesised from the clutter PS estimate and the knowledge of the clutter PS locus at the range of interest. This step requires, for each range cell l of interest, a model of the clutter CM $\underline{R}_{c,l} = E\{\underline{y}_{c,l}\,\underline{y}_{c,l}^{\dagger}\}$, the expression of which also requires the knowledge of the true spatial SVs. It is thus important to note that the benefits of the RBC algorithm leading to an accurate estimate can only be obtained if we have knowledge of the true spatial SVs, or a good approximation thereof.

4 RBC algorithm with partially calibrated array

The problem addressed in this section is to obtain an accurate estimate of the I + N CM by means of the RBC algorithm in the presence of RD when the true spatial SVs cannot be obtained for all possible DOAs. The goal of the method presented here is thus to obtain approximations to the missing true spatial SVs under the conditions described in Section 2.

4.1 Nearest-neighbour scheme

Before describing the array interpolation based approximation scheme in Section 4.2, we describe a first-cut approach based on a nearest-neighbour (NN) scheme.

Let us assume that we require the true spatial SV $s_s^{\text{true}}(\nu_s(\theta_0, \phi_0))$ corresponding to a DOA (θ_0, ϕ_0) that is not available in $\mathcal{S}_d$. The NN scheme consists in using, instead of the missing $s_s^{\text{true}}(\nu_s(\theta_0, \phi_0))$, the s_s^{true} in $\mathcal{S}$ that corresponds to the DOA (θ, ϕ) in $\mathcal{S}_d$ closest to (θ_0, ϕ_0). More formally, the NN in $\mathcal{S}$ of $s_s^{\text{true}}(\nu_s(\theta_0, \phi_0))$ is the true spatial SV $s_s^{\text{true}}(\nu_s(\theta_{0,\text{NN}}, \phi_{0,\text{NN}}))$ belonging to $\mathcal{S}$ and verifying

$$(\theta_{0,\text{NN}}, \phi_{0,\text{NN}}) = \operatorname*{argmin}_{(\theta,\phi)\in\mathcal{S}_d} \sqrt{(\theta_0 - \theta)^2 + (\phi_0 - \phi)^2}$$

This is illustrated in Fig. 4.

The NN scheme combined with the RBC algorithm is denoted NN-RBC. This simple scheme has a reduced computational cost. However, it is likely to fail when $\Delta\phi$ and $\Delta\theta$ (defined in Fig. 2) increase as is shown in Section 5.

4.2 Array interpolation scheme

First, we restate briefly the principles of array interpolation. Second we describe how the conventional approach applies array interpolation in the context of calibration issues. Then, we present our approach.

4.2.1 Principles of array interpolation:
The principle of array interpolation is to design a linear transformation $\underline{\mathbf{T}}$ that allows one to compute the data that would have been received by a virtual array if this virtual array had been used instead of the real array. $\underline{\mathbf{T}}$ must map the real array manifold into the predefined virtual array manifold over a given 2D field of view (A field of view is defined as the cartesian product of an elevation-angle interval and an azimuth-angle interval.) Φ of limited size such that

$$\underline{\mathbf{T}}s_s^r(\theta, \phi) \simeq s_s^v(\theta, \phi), \quad \forall(\theta, \phi) \in \Phi \qquad (4)$$

where $s_s^r(\theta, \phi)$ and $s_s^v(\theta, \phi)$ are the spatial SVs of the real array and of the virtual array, respectively. The nature of these spatial SVs is discussed below. $\underline{\mathbf{T}}$ is obtained by solving the following
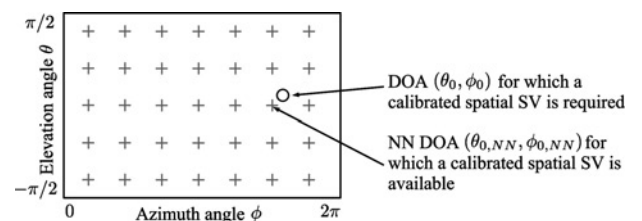
Figure 4 *Illustration of NN approximation scheme for missing true spatial SVs*

linear least-squares optimisation problem

$$\min_{\underline{\mathbf{T}}} \sum_{j=1}^{J} \|\underline{\mathbf{T}} \boldsymbol{s}_{\mathrm{s}}^{r}(\theta(j), \phi(j)) - \boldsymbol{s}_{\mathrm{s}}^{v}(\theta(j), \phi(j))\|_{2} \tag{5}$$
$$= \min_{\underline{\mathbf{T}}} \|\underline{\mathbf{T}} \underline{\mathbf{A}}^{r} - \underline{\mathbf{A}}^{v}\|_{F}$$

where the $(\theta(j), \phi(j))$'s, $j = 1, \ldots, J$, are the sample directions (defined later) in the field of view Φ, and F is the Frobenius norm. The matrices $\underline{\mathbf{A}}^{r}$ and $\underline{\mathbf{A}}^{v}$ contain the spatial SVs of the real array and of the virtual array as columns, respectively. The least-square solution of (5) is

$$\underline{\mathbf{T}} = \underline{\mathbf{A}}^{v} (\underline{\mathbf{A}}^{r})^{\dagger} (\underline{\mathbf{A}}^{r} (\underline{\mathbf{A}}^{r})^{\dagger})^{-1} \tag{6}$$

4.2.2 Conventional approach − Single mapping:
In the conventional approach [36], one chooses

• A single field of view Φ compatible with the zone over which the radar has to provide surveillance coverage (see Fig. 5a).

• The $\boldsymbol{s}_{\mathrm{s}}^{\mathrm{true}}$'s (corresponding to the DOAs simultaneously in $\mathcal{S}_{\mathrm{d}}$ and in Φ) as the real spatial SVs, that is, the $\boldsymbol{s}_{\mathrm{s}}^{r}$'s.

a

b
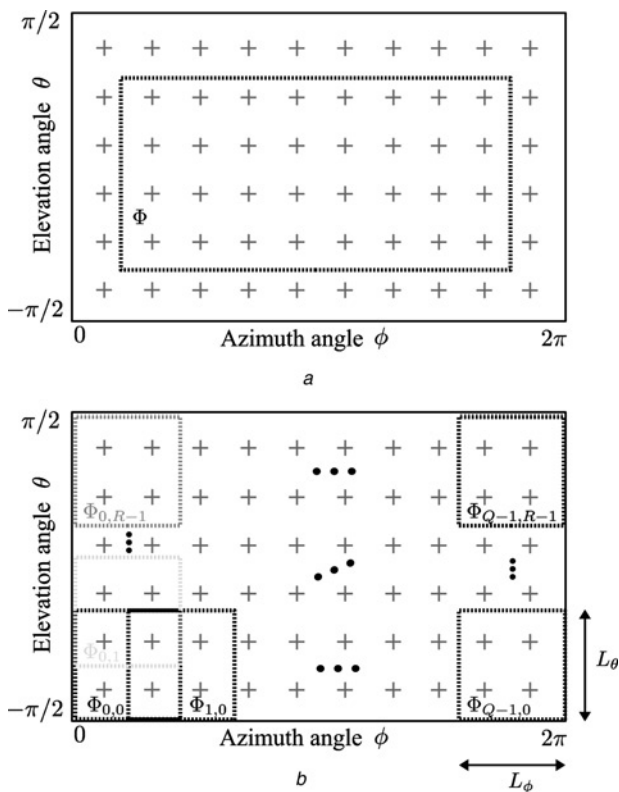
Figure 5 *Single mapping against multiple mappings*
a Conventional approach using array interpolation with a single field of view Φ
b Our approach using several fields of view $\Phi_{q,r}$, $q = 0, \ldots,$ $Q - 1$, $r = 0, \ldots, R - 1$

• The $\boldsymbol{s}_{\mathrm{s}}^{\mathrm{mod}}$'s (corresponding to the DOAs simultaneously in $\mathcal{S}_{\mathrm{d}}$ and in Φ) as the virtual spatial SVs, that is, the $\boldsymbol{s}_{\mathrm{s}}^{v}$'s.

The above elements are then used to compute a single $\underline{\mathbf{T}}$ by applying (6). The application of $\underline{\mathbf{T}}$ to the spatial part of the recorded snapshots (done by applying $\underline{\mathbf{I}}_{M} \otimes \underline{\mathbf{T}}$ to each snapshot, where $\underline{\mathbf{I}}_{M}$ is the identity matrix of size M) would yield virtual snapshots for which the $\boldsymbol{s}_{\mathrm{s}}^{\mathrm{mod}}$'s could then act as true spatial SVs for any DOAs. Indeed, the virtual snapshot behaves as if it had been received by an array that behaves according to the $\mathcal{M}(\cdot, \cdot)$ used. This approach is appealing since now the 'true' virtual spatial SVs are available for every DOA in the RBC algorithm since they can be generated by the $\mathcal{M}(\cdot, \cdot)$ under consideration for generating the $\boldsymbol{s}_{\mathrm{s}}^{\mathrm{mod}}$'s.

Unfortunately, this method will fail when applied in the context of CAAs. Indeed, CAAs may provide surveillance coverage over an interval in azimuth as large as 360°. The contributions to a clutter snapshot recorded by a CAA may thus come from a very large field of view. However, the field of view over which $\underline{\mathbf{T}}$ correctly maps the real array manifold into the virtual array manifold is relatively small, even if we use more elaborate techniques for the design of the virtual array, as shown in [37]. This implies that applying $\underline{\mathbf{I}}_{M} \otimes \underline{\mathbf{T}}$ to the clutter snapshots will fail to produce an accurate virtual snapshot. It thus appears inappropriate to apply the same mapping $\underline{\mathbf{T}}$ to all the spatial SVs making up the snapshot to be transformed.

4.2.3 Our approach − multiple mappings:
The solution we propose is motivated by the nature of the RBC algorithm. Both in the estimation of the clutter PS and in the synthesis of the CM estimate, the spatial SVs used are accessed individually. This means that different $\underline{\mathbf{T}}$'s might be computed and applied to different spatial SVs. These observations led us to devise the following approach.

Instead of looking for an overall transformation $\underline{\mathbf{T}}$ to be applied to the spatial part of the data snapshots, we choose

• Several fields of view $\Phi_{q,r}$, $q = 0, \ldots, Q - 1$, $r = 0, \ldots, R - 1$ instead of a single field of view Φ.

• The $\boldsymbol{s}_{\mathrm{s}}^{\mathrm{true}}$'s (corresponding to the DOAs simultaneously in $\mathcal{S}_{\mathrm{d}}$ and in the union of the $\Phi_{q,r}$'s) as the virtual spatial SVs, that is, the $\boldsymbol{s}_{\mathrm{s}}^{v}$'s, which is the opposite of what is done in the conventional approach.

• The $\boldsymbol{s}_{\mathrm{s}}^{\mathrm{mod}}$'s (corresponding to the DOAs simultaneously in $\mathcal{S}_{\mathrm{d}}$ and in the union of the $\Phi_{q,r}$'s) as the real spatial SVs, that is, the $\boldsymbol{s}_{\mathrm{s}}^{r}$'s, which is also the opposite of what is done in the conventional approach.

Carefully note that we are not going to apply the $\underline{\mathbf{T}}_{q,r}$ to the snapshots as in the conventional approach, but that we are going to approximate the missing $\boldsymbol{s}_{\mathrm{s}}^{\mathrm{true}}$'s. That is why we use the $\boldsymbol{s}_{\mathrm{s}}^{\mathrm{true}}$'s as the $\boldsymbol{s}_{\mathrm{s}}^{v}$'s and the $\boldsymbol{s}_{\mathrm{s}}^{\mathrm{mod}}$'s as the $\boldsymbol{s}_{\mathrm{s}}^{r}$'s. The

benefit of this approach is that we can let the size of the fields of view over which each $\underline{\underline{\mathbf{T}}}_{q,r}$ operates be a free parameter. Details are as follows.

First, we define several fields of view $\Phi_{q,r}$ as shown in Fig. 5b. The size in azimuth, L_ϕ, and the size in elevation, L_θ, are kept as free parameters to be determined. The L_ϕ's of all $\Phi_{q,r}$'s are assumed identical. The same is true for the L_θ's. However, L_θ may differ from L_ϕ. The position of the centre of each $\Phi_{q,r}$ is such that it overlaps with half of $\Phi_{q-1,r}$ and half of $\Phi_{q+1,r}$. The same is true in elevation. This ensures that no s_s^{mod} to be mapped is ever located at the border of a field of view. Indeed, the performance of array interpolation is generally worse at the border of the field of view than it is at its centre [37].

Second, for each $\Phi_{q,r}$, we find the corresponding $\underline{\underline{\mathbf{T}}}_{q,r}$ by minimising

$$\min_{\underline{\underline{\mathbf{T}}}_{q,r}} \sum_{i=1}^{I} \| \underline{\underline{\mathbf{T}}}_{q,r} s_s^{\text{mod}}(\theta(i), \phi(i)) - s_s^{\text{true}}(\theta(i), \phi(i)) \|_2 \quad (7)$$

where $(\theta(i), \phi(i)) \in \Phi_{q,r}$, $i = 1, \ldots, I$, are the sample directions taken now in the field of view under consideration. These directions correspond to the DOAs for which s_s^{true}'s are available, that is, the DOAs in $\mathcal{S}_d$.

Third, we approximate the missing s_s^{true}'s as follows. Let us assume again that we require the true spatial SV $s_s^{\text{true}}(v_s(\theta_0, \phi_0))$ corresponding to some DOA (θ_0, ϕ_0) needed in the RBC algorithm. Instead of using $s_s^{\text{mod}}(\theta_0, \phi_0)$, we compute an approximation $\tilde{s}_s^{\text{true}}(\theta_0, \phi_0)$ to $s_s^{\text{true}}(\theta_0, \phi_0)$. To do so, we first determine the $\Phi_{q,r}$ with centre closest to the given DOA (θ_0, ϕ_0). Then, we apply the corresponding $\underline{\underline{\mathbf{T}}}_{q,r}$ to $s_s^{\text{mod}}(\theta_0, \phi_0)$ to obtain

$$\tilde{s}_s^{\text{true}}(\theta_0, \phi_0) = \underline{\underline{\mathbf{T}}}_{q,r} s_s^{\text{mod}}(\theta_0, \phi_0) \quad (8)$$

$\tilde{s}_s^{\text{true}}(\theta_0, \phi_0)$ is then used as a surrogate for the missing $s_s^{\text{true}}(\theta_0, \phi_0)$.

This array interpolation based approximation scheme is an extension of the one presented in [38], where the parameter L_θ of the field of views was kept fixed. L_θ was considered to be imposed by the range interval over which the radar system has to provide surveillance coverage, which may be difficult if the range interval is large.

4.3 Extension of RBC algorithm to partially calibrated arrays

We can now extend the RBC algorithm summarised in Section 3.2. (A) In the analysis step, we proceed as follows to accurately compute a PS estimate at a given range cell for a specific $(v_s(\theta, \phi), v_d)$-pair. Instead of using $s_s^{\text{mod}}(\theta, \phi)$, we compute the approximation $\tilde{s}_s^{\text{true}}(\theta, \phi)$ as described above. (B) The registration step remains unchanged. (C) In the synthesis

step, we proceed in the same fashion to obtain the $\tilde{s}_s^{\text{true}}(\theta, \phi)$'s required to form the CM estimate. The array interpolation scheme combined with RBC is denoted AI-RBC.

5 Results

In the absence of real measurements, the true spatial SVs and each datacube must be generated synthetically, that is, from a model. Two such models will be considered for generating the s_s^{true}'s. First, we consider a simple analytical model (Section 5.1). Second, we consider a more realistic model obtained by the numerical electromagnetic tool FEKO [33] (Section 5.2). The parameters common to all simulations are as follows. We use a clutter-to-noise ratio of 20 dB, a wavelength of 0.03 m, $M = 12$ pulses and $L = 20$ secondary snapshots. The secondary snapshot are located at the BS ranges $R_b = 18 + 0.6k$ (in kilometres), $k = 0, \ldots, 19$. For the temporal decorrelation, we use a Gaussian CM taper with a spectral standard deviation of $\sigma_v = 0.5$ m/s as suggested in [9]. Spatial decorrelation is not considered here. The parameters for the BS flight configuration used in the simulations are $x_R = 7$ km, $y_R = 3$ km, $z_R = -2$ km, $v_T = 120$ m/s, $v_R = 90$ m/s, $\alpha_R = 30°$, $\delta = 10°$ and $H = 8$ km (which is the altitude of the transmitter above ground).

As indicated in Section 2, we assume throughout that the s_s^{mod}'s are generated by $\mathcal{M}(\cdot, \cdot)$ with the general functional form given by (3). Here, we consider, for both Sections 5.1 and 5.2, a particular case of (3) obtained by setting the gains $g_n(\theta, \phi)$ to unity, that is

$$s_s^{\text{mod}}(v_s) = \left[e^{j(2\pi v_s^T p(0))/(\lambda/2)} \cdots e^{j(2\pi v_s^T p(N-1))/(\lambda/2)} \right]^T \quad (9)$$

The results will show that our solution based on the s_s^{mod}'s generated by (9) allows one to minimise the modelling effort for the s_s^{mod}'s, while still having very promising STAP performance.
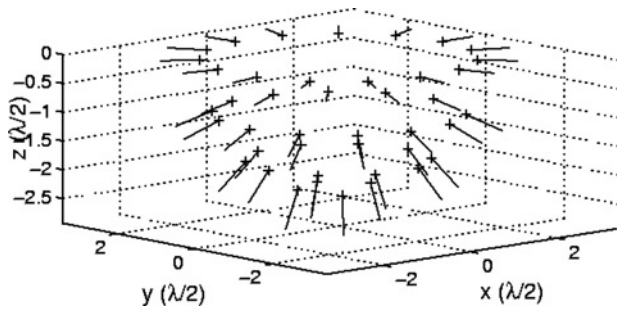
5.1 Simple analytical model

The first array used to evaluate the end-to-end performance of our algorithm is a bowl-shaped array with $N = 42$ elements (Fig. 6). The array's s_s^{true}'s are computed according to

$$s_s^{\text{true}}(v_s) = \left[\sqrt{g_0^{\text{true}}(\theta, \phi)} e^{j(2\pi v_s^T p(0))/(\lambda/2)} \right.$$
$$\left. \cdots \sqrt{g_{N-1}^{\text{true}}(\theta, \phi)} e^{j(2\pi v_s^T p(N-1))/(\lambda/2)} \right]^T$$

where the antenna gains are given by

$$g_n^{\text{true}}(\theta, \phi) = \begin{cases} G_0 \cos^2\left[\dfrac{\alpha_n(\theta, \phi)\pi}{\theta_0}\right] & \text{if } -\dfrac{\pi}{2} \le \alpha_n(\theta, \phi) \le \dfrac{\pi}{2} \\ G_0 G_B \cos^2\left[\dfrac{\alpha_n(\theta, \phi)\pi}{\theta_0}\right] & \text{if } \dfrac{\pi}{2} < \alpha_n(\theta, \phi) < \dfrac{3\pi}{2} \end{cases}$$

Figure 6 *Bowl-shaped CAA with N = 42 elements*

The short line segments represent the normals to the surface subtending the array. Axes are in units of $\lambda/2$

where $\alpha_n(\theta, \phi)$ is the angle between the DOA and the normal to the surface subtending the array at the nth antenna element, G_0 is the gain value in the direction of maximum gain, G_B is the backlobe attenuation and θ_0 parametrises the first-null beamwidth of the antenna.

Fig. 7 shows SINR loss (SINRL) [1] curves as a function of ν_d for two sets of values for the quadruplet $(\Delta\theta, \Delta\phi, L_\theta, L_\phi)$ and for two DOAs chosen in the range cell under

examination. The left column corresponds to calibration steps given by $(\Delta\theta, \Delta\phi) = (10°, 10°)$ and a field-of-view size given by $(L_\theta, L_\phi) = (40, 160)$, whereas the right column corresponds to $(\Delta\theta, \Delta\phi) = (15°, 15°)$ and $(L_\theta, L_\phi) = (60°, 240°)$. Each row corresponds to a different DOA in the range cell under examination. Each subfigure shows the SINRL curves for distinct algorithms. The usual references are shown, that is, the OP and the SMI [5]. As additional references, we show the SINRL curves of the RBC algorithm having access to the s_s^{true}'s for all (θ, ϕ)'s and the SINRL curves of the RBC algorithm having access only to the s_s^{mod}'s (for any DOA) and no access to any s_s^{true}. These algorithms are denoted True-RBC and Nom-RBC, respectively. Of course, we also show the SINRL curves for NN-RBC and for AI-RBC.

True-RBC performs almost as well as the OP [35], [15], since their SINRL curves are seen to be almost superimposed. In all cases, the Nom-RBC algorithm fails to give satisfactory performance. This is to be expected since the modelling effort is kept small. For $(\Delta\theta, \Delta\phi) = (10°, 10°)$, NN-RBC still gives satisfactory performance, whereas AI-RBC performs almost as well as OP and True-RBC, since all three curves are almost superimposed. For $(\Delta\theta,$
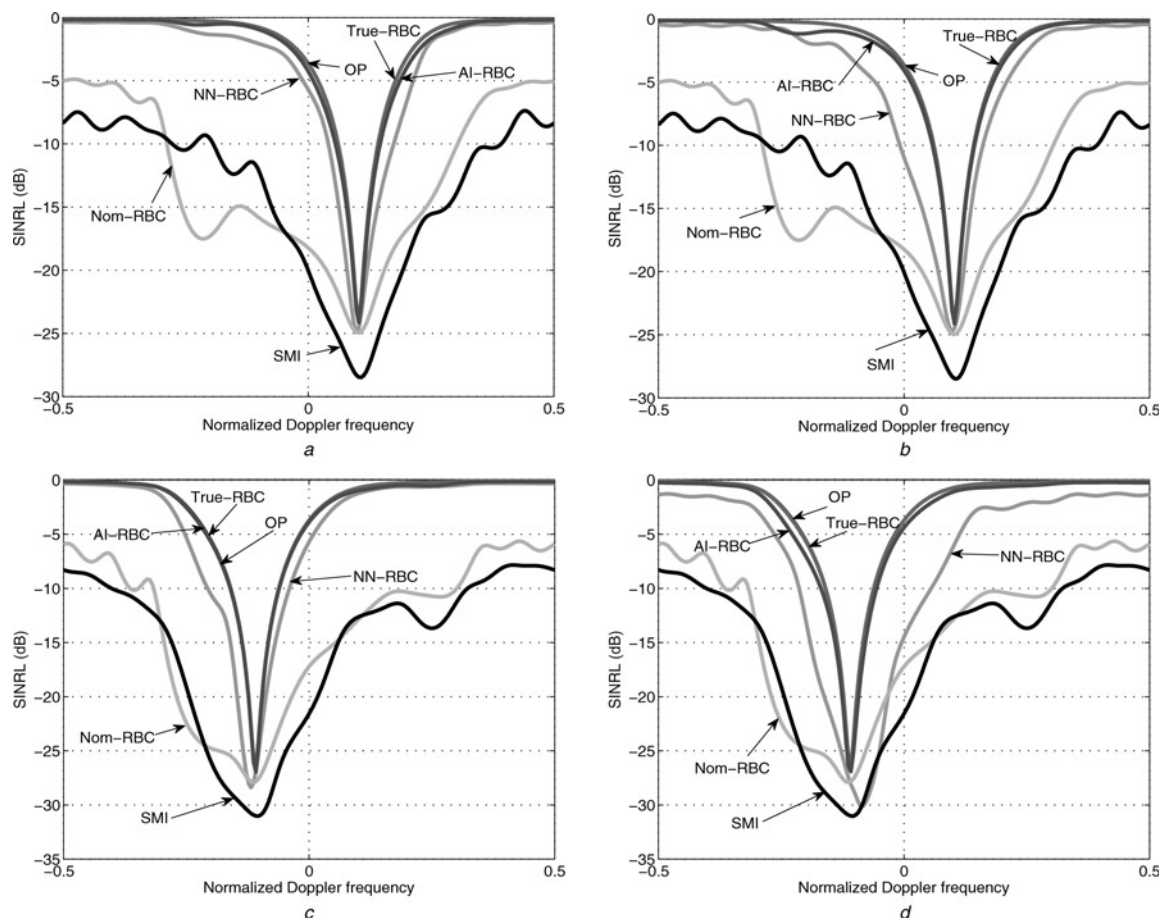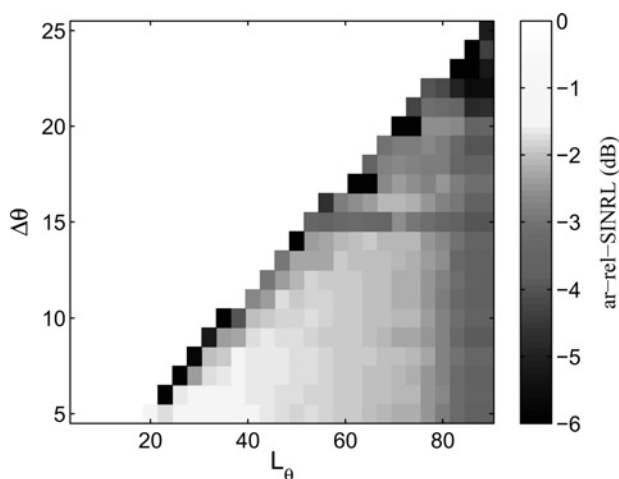

Figure 7 *SINRL curves for the array of Fig. 6 with $G_0 = 1$, $G_B = 0.01$ and $\theta_0 = \pi$*

The left and right columns correspond to $(\Delta\theta, \Delta\phi, L_\theta, L_\phi) = (10°, 10°, 40°, 160°)$ and $(\Delta\theta, \Delta\phi, L_\theta, L_\phi) = (15°, 15°, 60°, 240°)$, respectively. Each row corresponds to a different DOA in the range cell under examination

$\Delta\phi$) = (15°, 15°), NN-RBC becomes unreliable, but AI-RBC still gives excellent performance. We thus clearly see the benefit of AI-RBC.

To investigate further the impact of the parameters $\Delta\theta$, $\Delta\phi$, L_θ and L_ϕ, we introduce the average relative SINR loss, denoted ar-rel-SINRL. We define the relative SINR loss, denoted rel-SINRL, as the ratio of the SINRL of the algorithm under consideration, here AI-RBC, and the SINRL of the OP. We also define the ar-rel-SINRL for a given DOA as the average of the rel-SINRL over all the ν_d's. Fig. 8 shows the ar-rel-SINRL for the AI-RBC method at the DOA corresponding to Fig. 7a. It shows the average loss with respect to the OP because of the CM estimation under the hypotheses of a partially calibrated array. The white upper-left part corresponds to values of the quadruplet ($\Delta\theta$, $\Delta\phi$, L_θ, L_ϕ) for which no $\underline{\underline{\mathbf{T}}}_{q,r}$ can be computed. Indeed, for a given ($\Delta\theta$, $\Delta\phi$), the size of the field of view must cover a certain extent to have enough columns in the matrix $\underline{\mathbf{A}}^r$ for the system $\underline{\mathbf{A}}^r (\underline{\mathbf{A}}^r)^\dagger$ to be invertible as required by (6).

We observe that, for a given size of the field of view, the performance decreases as $\Delta\theta$ and $\Delta\phi$ increase. Indeed, the smaller the number of calibrated spatial SVs, the more difficult it is to estimate correctly the clutter CM. For a given ($\Delta\theta$, $\Delta\phi$), there exists an optimum size of the field of view. For too small a size of the field of views, the $\underline{\underline{\mathbf{T}}}_q$'s correctly map only the s_s^{mod}'s for which the corresponding s_s^{true}'s are known. This occurs if the number of calibrated DOAs in a given $\Phi_{q,r}$ is such that the system in (7) can be solved exactly, rather than in the least-square sense. In such a case, the mapping between the s_s^{mod}'s and the corresponding s_s^{true}'s for calibrated DOAs is exact, but totally erroneous for intermediate DOAs as $\underline{\underline{\mathbf{T}}}_{q,r}$ is not
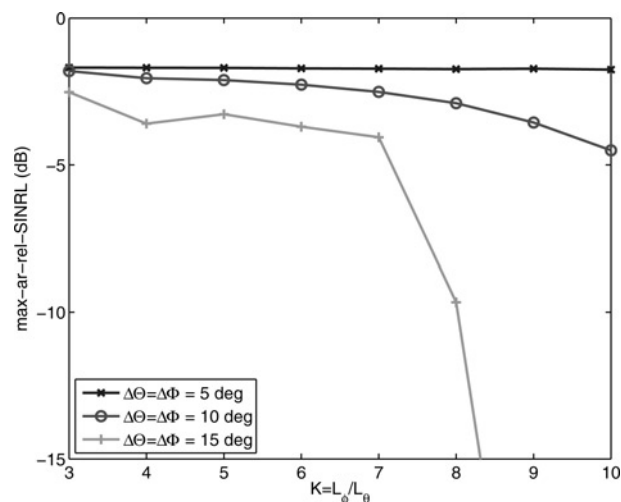
forced to take them into account to provide a low least-square error in (7). For too large a size of the field of views the angular extent of the $\Phi_{q,r}$'s becomes too large for the linear transformations $\underline{\underline{\mathbf{T}}}_{q,r}$ to perform a correct mapping between the s_s^{mod}'s and the corresponding s_s^{true}'s. This is the same problem as described in Section 4.2.1. Note that AI-RBC gives very promising performance over a fairly large region of the parameter space.

In Fig. 8, the shape of the field of fiew is fixed by the ratio $L_\phi/L_\theta = 4$. To investigate the influence of the shape of the field of view, we proceed as follows. The following description is for a given pair ($\Delta\theta$, $\Delta\phi$). We define the ratio

$$K = L_\phi/L_\theta \qquad (10)$$

as the shape parameter of the field of view. We also define the maximum, average, relative SINRL, denoted, max-ar-rel-SINRL, which is the maximum value of the ar-rel-SINRL obtainable by changing L_ϕ (L_θ changes accordingly through (10)). Fig. 9 shows the max-ar-rel-SINRL as a function of K for several ($\Delta\theta$, $\Delta\phi$) pairs.

We observe that, for a given ($\Delta\theta$, $\Delta\phi$), the smaller the ratio K, the higher the value of max-ar-rel-SINRL. Hence, the more the shape of a field of view approaches that of a square, the better the performance. This can be explained as follows. For large values of K, a field of view has the shape of a narrow rectangle. For such a field of view, there are more s_s^{mod}'s corresponding to DOAs located far away from the centre of the field of view than for a field of view with a shape closer to that of a square. However, for DOAs located away from the centre of the field of view the mapping is generally worse than for DOAs closer to the centre [37]. This explains why the performances for small values of K are better than for larger values of K.


Figure 8 *Average, relative SINRL, denoted ar-rel-SINRL, in dB, as a function of $\Delta\theta$ and L_θ*

Note that, to obtain a 2D colour-coded graph, we fixed $\Delta\phi$ to $\Delta\phi = \Delta\theta$ and L_ϕ to $L_\phi = 4L_\theta$. The white upper-left area corresponds to quadruplets ($\Delta\theta$, $\Delta\phi$, L_θ, L_ϕ) for which $\underline{\underline{\mathbf{T}}}_{q,r}$ cannot be computed (see text)

Figure 9 *Maximum average, relative SINRL, denoted max-ar-rel-SINRL, in dB, as a function of K*

5.2 More realistic model, based on FEKO

The second array used to evaluate the end-to-end performance of our algorithm is a quarter-sphere array with $N = 48$ elements (Fig. 10). The full sphere acts as the ground plane. The array's s_s^{true}'s were computed using the numerical electromagnetic tool FEKO, taking into account the mutual coupling among elements, as well as the interaction with the carrying platform acting as a ground plane. A given $s^{\text{true}}(\theta, \phi)$ is obtained as follows. We simulate a plane wave with unit-amplitude electric field impinging from direction (θ, ϕ) on the array under consideration. FEKO uses the method of moments (MoM) [39] to obtain the complex voltages at the output of the antenna elements. From these complex voltages, we immediately obtain the elements of $s^{\text{true}}(\theta, \phi)$.

Fig. 11 shows SINRL curves as a function of ν_d. Again, we clearly see the benefit of AI-RBC, which gives very promising performance, since its SINRL curves are seen to be almost superimposed with those of OP and True-RBC.
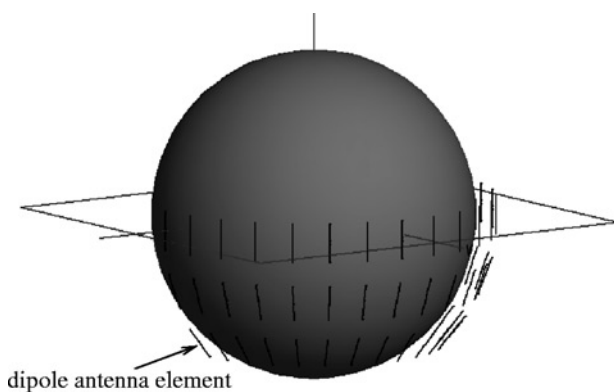
Figure 10 *Quarter-sphere array with N = 48 elements, with full sphere shown acting as ground plane*
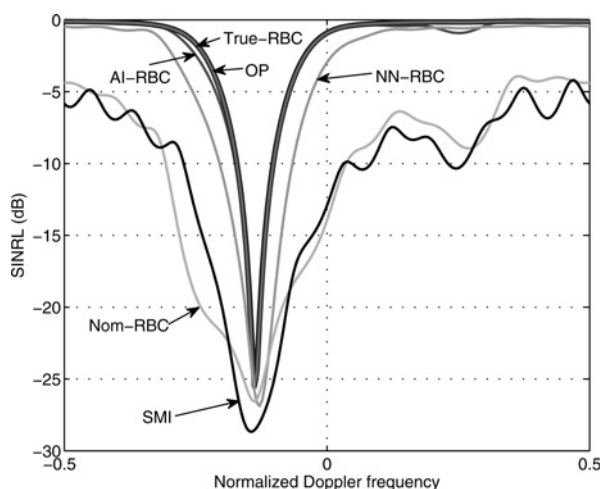
Figure 11 *SINRL curves for the array of Fig. 10 with ($\Delta\theta$, $\Delta\phi$, L_θ, L_ϕ) = (10°, 10°, 40°, 160°)*

6 Summary and conclusions

In this paper, we considered the problem of RD in STAP applied to CAAs that are only partially calibrated. We provided an innovative extension to the RBC algorithm of [4, 15] in order to obtain an estimate of the I + N covariance matrix even if the CAA is only partially calibrated.

In Section 2, we described a model of the signal recorded by a CAA. We also defined a partially calibrated array as an array for which the true spatial SV has been obtained in the calibration process (e.g. through measurements in an anechoic chamber) only for a some DOA of the incoming plane wave but not for all DOAs. In Section 3, we reviewed the RD problem and the RBC algorithm. Section 4 presents our innovative extension of the RBC algorithm. This extension is based on an array interpolation scheme that allows one to compute an approximation of the missing true spatial SVs, that is, the spatial SVs not obtained during the calibration phase of the array but required by the RBC algorithm and / or the STAP filter. In this way, the RBC algorithm can be used to estimate the I + N covariance matrix even if the array is only partially calibrated. Section 5 analysed the end-to-end performance on synthetic data. We tested our approach on, among other arrays, a quarter-sphere array placed in front of a metal sphere acting as a ground plane. The spatial SVs of this array were obtained using the electromagnetic simulation software FEKO, which accounts for the mutual coupling among the antenna elements and for the interaction with the metal sphere. We showed that, to obtain near optimum end-to-end performance, it is sufficient to obtain the true spatial SVs for only every 10° in elevation and every 10° in azimuth during the calibration process.

Future work should be aimed at improving the tiling of the calibration grid by the $\Phi_{q,r}$'s to reduce even further losses because of imperfect calibration.

7 Acknowledgment

8 References

[1] KLEMM R.: 'Principles of space–time adaptive processing', *IEE Radar, Sonar, Navig. Avionics*, 2002, **9**

[2] WARD J.: 'Space-time adaptive processing for airborne radar'. Technical Report 1015, MIT Lincoln Laboratory, Lexington, MA, 1994

[3] GUERCI J.: 'Space-time adaptive processing for radars' (Artech House, 2003)

[4] RIES P., LAPIERRE F.D., VERLY J.G.: 'RANSAC-based flight parameter estimation for registration-based range-dependence compensation in airborne bistatic STAP radar with conformal antenna arrays'. European Radar Conf., Manchester, UK, September 2006

[5] REED I., MALLETT J., BRENNAN L.: 'Rapid convergence rate in adaptive arrays', *IEEE Trans. Aerosp. Electron. Syst. (AES)*, 1974, **10**, (6), pp. 853–863

[6] MELVIN W.: 'Space-time adaptive radar performance in heterogeneous clutter', *IEEE Trans. Aerosp. Electron. Syst. (AES)*, 2000, **36**, (2), pp. 621–633

[7] GURRAM P., GOODMAN N.: 'Spectral-domain covariance estimation with a priori knowledge', *IEEE Trans. Aerosp. Electron. Syst.*, 2006, **42**, pp. 1010–1020

[8] MELVIN W., GUERCI J.: 'Knowledge-aided signal processing: a new paradigm for radar and other advanced sensor', *IEEE Trans. Aeros. Electron. Syst.*, 2006, **42**, pp. 983–996

[9] MELVIN W., SHOWMAN G.: 'An approach to knowledge-aided covariance estimation', *IEEE Trans. Aerosp. Electron. Syst.*, 2006, **42**, pp. 1021–1042

[10] BERGIN J., TEIXEIRA C., TECHAU P., GUERCI J.: 'Improved clutter mitigation performance using knowledge-aided space-time adaptive processing', *IEEE Trans. Aerosp. Electron. Syst.*, 2006, **42**, pp. 997–1009

[11] CAPRARO C., CAPRARO G., BRADARIC I., WEINER D., WICKS M., BALDYGO W.: 'Implementing digital terrain data in knowledge-aided space–time adaptive processing', *IEEE Trans. Aerosp. Electron. Syst.*, 2006, **42**, pp. 1080–1098

[12] BLUNT S., GERLACH K., RANGASWAMY M.: 'STAP using knowleddge-aided covariance estimation and the FRACTA algorithm', *IEEE Trans. Aerosp. Electron. Syst.*, 2006, **42**, pp. 1043–1057

[13] KLEMM R.: 'Comparison between monostatic and bistatic antenna configurations for STAP', *IEEE Trans. Aerosp. Electron. Syst. (AES)*, 2000, **36**, (2), pp. 596–608

[14] LAPIERRE F., VERLY J.: 'Registration-based method for range-dependence compensation in bistatic radar STAP operating on simulated stochastic snapshots', *EURASIP JASP J.*, 2005, **1**, pp. 85–98

[15] NEYT X., RIES P., VERLY J.G., LAPIERRE F.D.: 'Registration-based range-dependence compensation method for conformal array STAP'. Adaptive Sensor Array Processing Workshop, MIT Lincoln Laboratory, Lexington, MA, June 2005

[16] BORSARI G.: 'Mitigating effects on STAP processing caused by an inclined array'. IEEE National Radar Conf., Dallas, TX, May 1998

[17] HIMED B., ZHANG Y., HAJJARI A.: 'STAP with angle-Doppler compensation for bistatic airborne radars'. IEEE National Radar Conf., Long Beach, CA, May 2002

[18] MELVIN W., HIMED B., DAVIS M.: 'Doubly adaptive bistatic clutter filtering'. IEEE National Radar Conf., Hunstville, AL, May 2003

[19] MELVIN W., DAVIS M.: 'Adaptive cancellation method for geometry-induced nonstationary bistatic clutter environments', *IEEE Trans. Aerosp. Electron. Syst.*, 2007, **43**, (2), pp. 651–672

[20] PEARSON F., BORSARI G.: 'Simulation and analysis of adaptive interference suppression for bistatic surveillance radars'. Adaptive Sensor Array Processing Workshop, MIT Lincoln Laboratory, Lexington, MA, March 2001

[21] ZATMAN M.: 'Performance analysis of the derivative based updating method'. Adaptive Sensor Array Processing Workshop, MIT Lincoln Laboratory, Lexington, MA, March 2001

[22] JAFFER A., HIMED B., HO P.: 'Estimation of range-dependent clutter covariance by configuration system parameter estimation'. IEEE Int. Radar Conf., Arlington, VA, USA, May 2005

[23] RIES P., NEYT X., LAPIERRE F.D., VERLY J.G.: 'Fundamentals of spatial and doppler frequencies in radar STAP', *IEEE Trans. Aerosp. Electron. Syst. AES*, 2008, **44**, pp. 1118–1134

[24] RIES P., TEY S., LESTURGIE M., VERLY J.: 'New methodology for generating realistic data for evaluation of performance of radar stap algorithms'. Int. Radar Symp., Cologne, Germany, September 2007

[25] RIES P., NEYT X., DE GRÈVE S., LAPIERRE F.D., VERLY J.G.: 'Range-dependence compensation in STAP for arbitrary engagement geometries and receiver antenna arrays'. RTO-SET 095 Specialist Meeting, La Spezia, Italy, June 2006

[26] JAFFER A., HO P., HIMED B.: 'Adaptive compensation for conformal array STAP by configuration parameter estimation'. IEEE Radar Conference, Verona, NY, USA, April 2006

[27] NEYT X., ARCHEROY M., VERLY J.: 'Maximum likelihood range-dependence compensation for stap'. ICASSP, Honolulu, Hawaii, USA, April 2007

[28] NEYT X., DRUYTS P., ARCHEROY M., VERLY J.: 'Structured covariance matrix estimation for the range-dependent problem in STAP'. IASTED Int. Conf. Antennas, Radar, and Wave Propagation, Montreal, Canada, May 2007

[29] RIES P., LESTURGIE M., LAPIERRE F.D., VERLY J.G.: 'Knowledge-aided array calibration for registration-based range-

dependence compensation in airborne STAP radar with conformal antenna arrays'. European Radar Conference, Munich, Germany, October 2007

[30] BLUM R., MCDONALD K.: 'Analysis of STAP algorithms for cases with mismatched steering and clutter statistics', *IEEE Trans. Signal Process.*, 2000, **48**, pp. 301–310

[31] HERSEY R.: 'Adaptive detection and estimation using a conformal array antenna', PhD thesis (Georgia Institute of Technology, 2004)

[32] HERSEY R., MELVIN W., MCCLELLAN J.: 'Clutter limited detection performance of multi-channel conformal arrays', *Signal Process*, 2004, **84**, pp. 1481–1500

[33] EM Software & Systems-S.A. (Pty): 'FEKO - comprehensive EM solutions', Available at http://www.feko.info

[34] MELVIN W., CALLAHAN M., WICKS M.: 'Adaptive clutter cancellation in bistatic radar'. 34th Asilomar Conference on Signals, Systems, and Computer, Pacific Grove, CA, October–November 2000

[35] LAPIERRE F.D., VERLY J.G.: 'Computationally-efficient range-dependence compensation method for bistatic radar STAP'. IEEE National Radar Conf., Arlington, VA, May 2005

[36] KIM K., ZHANG Y., HAJJARI A., HIMED B.: 'A uniform planar virtual approach to conformal array STAP'. IEEE Int. Radar Conf. 2004, Toulouse, France, October 2004

[37] BÜHREN M., PESAVENTO M., BÖHME J.: 'Virtual array design for array interpolation using differential geometry'. ICASSP, Montreal, Canada, May 2004

[38] RIES P., LAPIERRE F.D., LESTURGIE M., VERLY J.G.: 'Range-dependence compensation in airborne bistatic STAP for partially calibrated conformal antenna arrays'. IEEE Radar Conference, Rome, Italy, May 2008

[39] DAVIDSON D.B.: 'Computational Electromagnetics for RF and microwave engineering' (Cambridge University Press, 2005)